Instability due to Viscosity Stratification Downstream of a Centerline Injector

Qing Cao, Amy L. Ventresca, K.R. Sreenivas and Ajay K. Prasad*

Department of Mechanical Engineering, University of Delaware, Newark, DE 19716, USA

A common injector geometry upstream of a static mixer is the centerline injector. A flow instability can arise due to viscosity differences between the injected core-flow and the outer co-flow. This instability can adversely affect the effectiveness of the mixing operation. An experimental investigation of miscible viscosity-stratified flow in a circular geometry was performed using Laser Induced Fluorescence (LIF) and Particle Image Velocimetry (PIV). The experimental results for the stable region agree with the analytical results. The unstable region exhibits different modes depending on the viscosity ratio, volume flux ratio, and Reynolds number. The modes include wavy core-flow with fissures and wavy core-flow with core breakup. The time-averaged experiment velocity profiles for the unstable core indicate a broadening of the jet at the centerline, which is consistent with the LIF visualization.

L'injecteur centré est une géométrie d'injection commune en amont des mélangeurs statiques. Une instabilité de l'écoulement peut survenir en raison des différences de viscosité entre l'écoulement piston injecté et le cocourant extérieur. Cette instabilité peut nuire à l'efficacité de l'opération de mélange. On a donc mené une étude expérimentale pour un écoulement biphasique miscible stratifié par la viscosité dans une géométrie circulaire basée sur la fluorescence induite par laser (LIF) et la vélocimétrie à imagerie de particules (PIV). Les résultats expérimentaux pour la région stable concordent avec les résultats analytiques. La région instable montre différents modes qui dépendent du rapport de viscosité, du rapport de flux volumique et du nombre de Reynolds. Ces modes comprennent l'écoulement piston à vagues avec fissures et l'écoulement piston avec vagues avec rupture du piston. Les profils de vitesse expérimentaux moyennés dans le temps pour le piston instable indiquent un élargissement du jet à la ligne de centre qui est cohérent avec la visualisation par LIF.

Keywords: static mixer, instability, viscosity stratified flow, LIF, PIV.

In recent years, the static mixer has been adopted for a large number of blending and dispersion operations. Static mixers, also known as motionless or in-line mixers, constitute a low-cost option for mixing in the chemical process industry. Static mixers offer attractive features such as closed-loop operation, and no moving parts, in contrast to continuously-stirred tank reactors (Streiff and Rogers, 1994). The two liquids to be mixed (for example, a polymer melt and an additive) are forced under high pressure through the mixer placed inside a tube, and the two liquids are cut and folded repeatedly as they negotiate the bends and openings within the mixer. The scale of segregation between the liquids is greatly reduced by this process such that eventually diffusion can complete the mixing process. The reduction in the scale of segregation is obviously dependent on the liquid properties, volume flux ratio, the number and type of mixing elements, and the inlet geometry. A typical inlet geometry to the static mixer is the centerline injector as depicted schematically in Figure 1.

Recently, industrial mixing experts (Guertin, 1997) expressed a concern about an unusual mixing behaviour of two miscible fluids. When a low-viscosity fluid is centrally injected into a co-flowing outer stream of high-viscosity fluid, it was conjectured that patches of unmixed fluid might remain despite passage through one or more sets of static mixers. Although radial mixing was assured, the same was not true for axial mixing. This phenomenon was attributed to an instability mechanism that operates downstream of the centerline injector for a particular viscosity ratio and volume flow rate ratio of the two streams.

This instability arises due to a discontinuity in the slope of the velocity profile, resulting from a mismatch of viscosity at the interface between the lower viscosity core-flow and the higher viscosity co-flow. The instability leads to a wavy oscillation of the core-flow as depicted schematically in Figure 1. It may be argued that for an extreme manifestation of this instability, the centrally injected stream might actually break up into axially segregated clumps leading to poor axial mixing downstream of the mixers. Our specific objective is to understand the instability mechanism as a function of viscosity ratio and volume flux ratio of the streams. We adopt the widely used circular geometry for our experiments and analysis. The flow of two miscible liquids inside a circular tube can be quite complex. In our experiments, several interfacial instability regimes have been observed for the first time.

Multi-layer viscosity stratified flow was first studied theoretically by Yih (1967), who considered two-layer plane Couette-Poiseuille flow of fluids

*Author to whom correspondence may be addressed. E-mail address: prasad@me.udel.edu

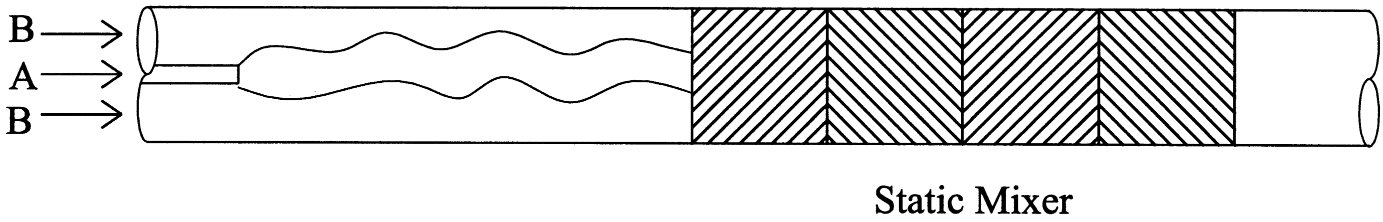

Figure 1. Centerline injector geometry for static mixing; instability is depicted immediately downstream of injector. Core-flow ≡ A; Co-flow ≡ B.

Table 1. Power-law parameters *K* and *n* in Figure 2.

Sample #	CMC concentration by weight	K (Pa·s^m)	n
1	0.42%	0.4925	0.7635
2	0.18%	0.1492	0.8064
3	0.06%	0.0289	1
4	0.03%	0.0089	1

with different viscosities. He performed a long-wave perturbation analysis in the absence of interfacial tension and reached the following significant conclusion: both plane Poiseuillle flow and plane Couette flow can be unstable for arbitrarily small Reynolds numbers due to viscosity stratification. Later Yih's method was applied by Hickox (1971) in axisymmetric vertical pipe flow of two fluids with different densities. He restricted his study to the case in which the viscosity of the core is less than the annulus and considered both axisymmetric and asymmetric disturbances to the primary flow. Two important conclusions were obtained: first, the primary flow was always unstable to either asymmetric or axisymmetric disturbances, and second, the primary cause of instability was the difference in viscosities of the two fluids.

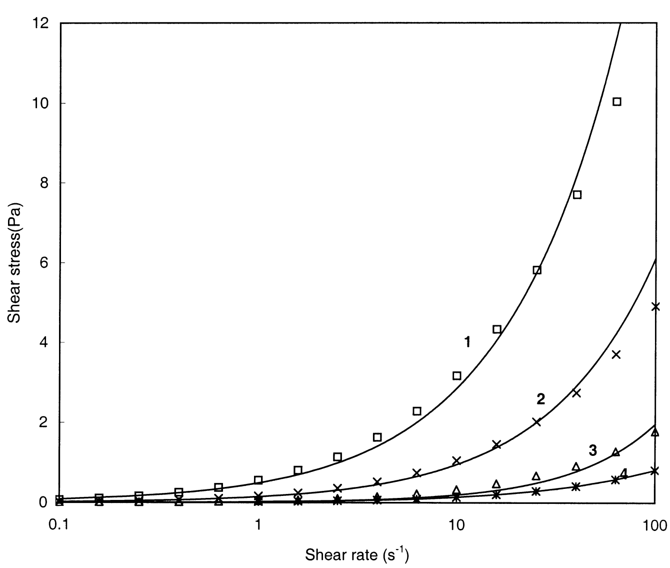

Figure 2. Shear stress versus strain rate for various CMC solutions at 25°C.

Joseph et al. (1984) extended Hickox's study by considering lubricated pipelining in which the core viscosity is greater than the annulus viscosity. They showed that the lubricated flows could be stable. Multi-layer flow has been a topic of many other theoretical investigations (Li, 1969; Renardy and Joseph, 1985; Charru and Fabre, 1994; Ranganathan and Govindarajan, 2001).

In contrast to the relatively large number of theoretical investigations, very few experimental studies have addressed the problem of multi-layer viscosity stratified flow. Charles et al. (1961) investigated the horizontal flow of equal density oil-water mixtures in a 26.4 mm diameter pipe. A series of flow patterns was observed as the oil flow rate was decreased but the water flow rate held constant. The flow pattern changed from water-drops-in-oil, oil-in-water-concentric, oil-slugs-in-water and oil-bubbles-in-water, to oil-drops-in-water. The slight density differential between the oil and the water was believed to cause the resulting unstable flow patterns of oil-slugs-in-water and oil-bubbles-in-water. Similar flow patterns were observed in the experiments of vertical flow of motor oil and water performed by Bai et al. (1992). Besides those patterns which were observed in horizontal pipes, they found that there existed at least two more patterns: bamboo waves and intermittent corkscrew waves. Channel flow stability experiments were performed by Kao and Park (1972). They developed a device that could introduce disturbances of different wavelengths at the interface. Their experiments showed that all small disturbances were damped when the water Reynolds number was smaller than the critical value of 2300. For the water Reynolds numbers above the critical value, disturbances at the oil-water interface of the water and oil began to grow. Moreover, when the water Reynolds numbers were bigger than the critical value, it was shown that interfacial waves could be observed even without artificial excitation.

So far, experimental studies have limited their scope to immiscible fluids (in the presence of interfacial tension) with high-viscosity annulus flows, and do not address the case under consideration in this study. The goal of this research is to examine instabilities in miscible liquids with a lower-viscosity core-flow surrounded by a higher viscosity co-flow.

Experimental Set-up

The two liquids used in this investigation were prepared by dissolving suitable amounts of carboxymethyl cellulose (CMC) powder in water to obtain solutions of desired viscosities. Even small amounts of CMC can increase the viscosity of the solution dramatically. For all the cases studied here, the CMC content in water is smaller than 1%. Our viscosity measurements indicate

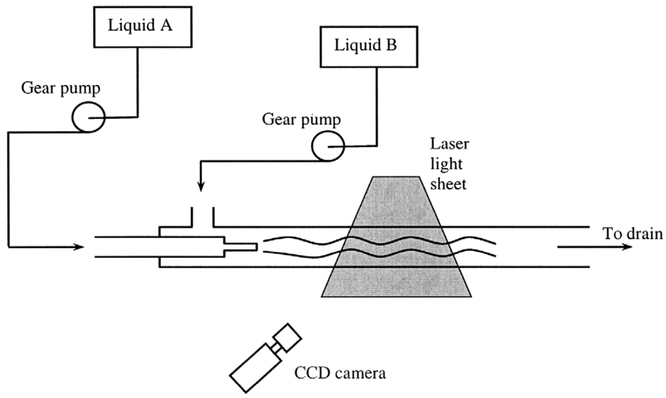

Figure 3. Experimental set-up.

a slight shear-thinning behaviour even for such low CMC concentrations. We use a power-law model $\tau = K(du/dr)^n$ to characterize the CMC solution, where τ is the stress, K and n are power-law coefficients, and du/dr is the strain rate. Viscosity data as a function of strain rate were obtained using a Rheometrics Dynamic Stress Rheometer (model #SR-5000). The stress curves for CMC solutions with various percentages of Hercules Aqualon 7H4F grade CMC at 25 degrees Celsius are shown in Figure 2. Power-law parameters for various samples were obtained by curve fitting and are shown in Table 1.

During experiments, the densities of the two liquids comprising the inner core-flow and the outer co-flow were carefully matched by adding sugar to the lower viscosity liquid. The primary reason for density-matching is to eliminate the influence of density differences and isolate the effect of viscosity stratification. Additionally, density-matching allowed a horizontal set-up for the experiment. Similarly, the use of aqueous solutions of CMC for both streams reduced the influence of interfacial tension in the problem. As an example, the interfacial tensions across two density-matched liquids with 0.03% and 0.42% CMC by weight, and 0.06% and 0.18% CMC by weight were obtained as 1.8×10^{-3}N/m and 1.0×10^{-3}N/m, respectively, using a Krüss GmbH Digital Tension Meter (model K 10T). The corresponding Weber number ($\rho U^2 D/\gamma_t$, where ρ is the liquid density, U is the nominal velocity through the test-section, D is the test-section diameter, and γ_t is the interfacial tension) for our experiments is of order 1. Therefore, although the effect of interfacial tension is not negligible, it is also not the dominant force in this problem.

CMC solutions can exhibit viscoelastic behaviour that can influence the instability under investigation. We performed a check for viscoelasticity and confirmed that this effect was indeed negligible for the CMC concentrations used in this study. For example, let us consider the case of the highest CMC (by weight) solution that was used in our experiments (0.42%). The plots for G' (storage modulus) and G'' (loss modulus) indicate a crossover at a frequency of 100 Hz (relaxation time τ = 0.01 sec). Using our typical flow parameters (flow time constant t_f = 12 sec), we estimate the corresponding Deborah number (τ/t_f) as 0.001. This confirms that viscoelastic behaviour is not significant in our problem.

Figure 3 shows the experimental set-up of the study. The two liquids were stored in supply tanks. Two gear pumps (Zenith, model BMC-5337 and BPB-4391) delivered the two liquids separately to the inlet region of the pipe where they were injected concentrically by means of a nozzle so that the lower viscosity liquid was introduced as a core-flow inside a higher viscosity annular co-flow. The diameter of the injector nozzle was 1.75 mm. A single motor (Graham, model 6008) operating between 10 and 70 rpm simultaneously drove both pumps. The small gear pumped fluid at 3.0 ml per revolution, while the large gear pumped fluid at 16.7 ml per revolution. Small/small and small/large gear combinations were used. The test section consisted of a Plexiglas tube, which is smooth and transparent with an internal diameter of 25.4 mm. Laser Induced Fluorescence (LIF) was used to visualize the instability, and Particle Image Velocimetry (PIV) was used to obtain instantaneous, two-dimensional velocity data along an axial plane. All the frames were recorded 76 mm downstream from the nozzle.

Laser Induced Fluorescence (LIF)

LIF is a visualization technique that exploits fluorescence produced when laser illumination at a specific wavelength excites dye molecules that have been added to the flow. The liquid stream emerging from the centerline injector has a small amount of fluorescing dye (Rhodamine 6G) homogeneously mixed with it, while the co-flow is transparent. As shown in Figure 3, longitudinal cross-sections (containing the tube axis) are illuminated with laser light (frequency-doubled Nd:YAG laser producing green light at 532 nm) formed into a 1 mm-thick sheet, and the resulting fluorescence is captured on a high-resolution Kodak ES 1.0 CCD camera (1k × 1k pixels). At low-dye concentrations, the intensity of fluorescence is proportional to the local dye concentration, and therefore to the local concentration of the injected liquid. This technique is extremely effective in demarcating the injected liquid from the co-flow and can therefore be used to visualize the flow patterns emerging from the centerline injector.

A potential concern about using dye to demarcate the interface is that the diffusivity of Rhodamine dye across the interface may be different from that of CMC; in fact, Rhodamine dye with its smaller molecular weight will diffuse faster than CMC as predicted by the Stokes-Einstein equation. However, the Peclet number based on the current flow parameters and dye diffusivity is about 10^4 (see Ventresca et al., 2002). Therefore, the dyed fluid transits our test-section so rapidly that diffusion is virtually negligible. The implication is that, although the dye diffuses faster than CMC, it still diffuses much too slowly to be significant in this work. Therefore, the dye indeed provides an accurate demarcation of the interface.

Particle Image Velocimetry (PIV)

PIV is a well known technique for obtaining global velocity information, instantaneously and with high accuracy (Prasad, 2000). In contrast to point-wise techniques such as Laser Doppler Anemometry (LDA), PIV is a whole-field technique, and offers the advantage of instantaneous velocity data over extended domains.

PIV is a logical extension of classical flow visualization, which can only provide a qualitative view of the flow. In contrast, PIV provides high-resolution quantitative data about the velocity field. There are two stages in PIV: (1) recording, and (2) interrogation. In the recording stage the flow field is seeded with tracer particles small enough to follow the fluid streamlines. The tracer particles are illuminated by two successive bursts of laser light,

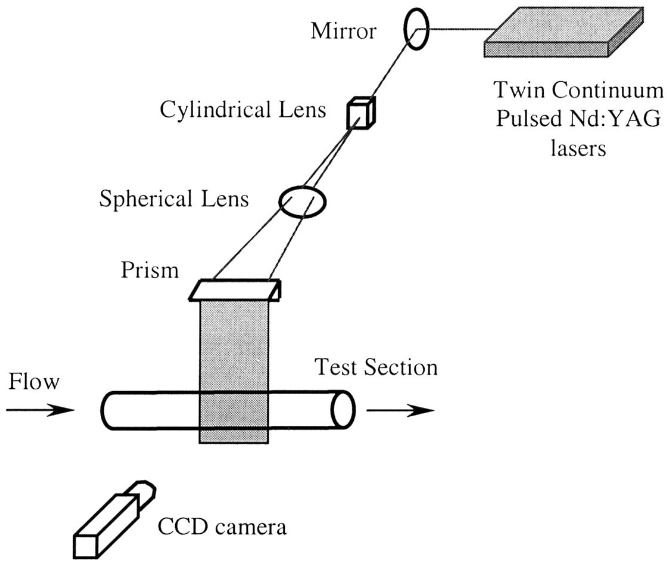

Figure 4. Particle image velocimetry.

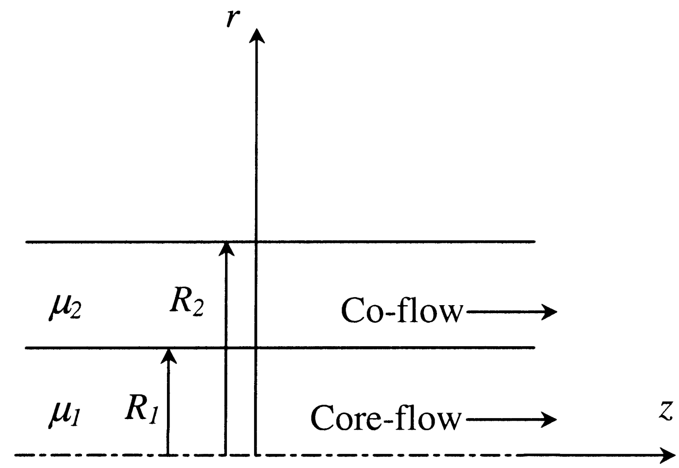

Figure 5. Flow geometry under consideration.

therefore, each particle casts two images on the recording medium. The laser illumination is formed into a sheet about 1 mm thick, so the time separation between pulses has to be small enough to retain the particle inside the sheet during both pulses.

During interrogation, the PIV image frame containing hundreds of thousands of image pairs is processed using Fast Fourier Transform (FFT) based correlation techniques to extract the velocity field. Our software determines the displacement of small groups of particle images called interrogation spots by calculating the spatial cross-correlation between one spot, and a second spot displaced from the first by the estimated local displacement vector. The location of the maximum in the cross-correlation function provides the *x* and *y* components of velocity. The typical size of an interrogation spot is 1 mm; however, by increasing the recording magnification, the interrogation spot size can be greatly reduced allowing for even higher resolution. Each interrogation spot yields one vector whose value corresponds to the average velocity of all the particles contained within that measuring volume. Interrogation spots (and so also velocity vectors) are located on a Cartesian grid.

Our PIV facilities include twin Nd:YAG Continuum Surelite II pulsed lasers (300 mJ/pulse at 10 Hz), a Kodak 1.0 ES digital camera, and custom-built PIV hardware with associated control and triggering electronics, and software. PIV tracer particles consisting of 8 μm diameter, hollow glass spheres were mixed thoroughly with both liquids to a concentration of 10 to 20 particles/mm^3. The laser beam was formed into a sheet using a sheet forming module and directed downwards such that it contains the pipe axis. The pipe is enclosed within a rectangular box filled with the working fluid to remove optical distortions at the cylindrical surface of the pipe (refractive-index matching). The camera is fully synchronized with the pulsing laser sheets and views the illuminated plane in an orthogonal manner.

The camera records particle images at two successive instants in time in order to extract the velocity over the planar two-dimensional domain. The range of spatial scales that can be resolved is about 30. Figure 4 depicts the experimental set-up for PIV recording.

Results and Discussion

Primary Flow

Figure 5 depicts the flow geometry under consideration. We consider two liquids that are co-flowing concentrically inside a circular pipe. The inner liquid (core-flow) extends up to a radius of R_1 and has a volume flux of Q_1 and power-law coefficients K_1 and n_1. The outer liquid flows in the annular gap, $R_1 \le r \le R_1$ with a volume flux Q_2, and power-law coefficients K_2 and n_2. For the following analysis, the two fluids are constrained from mixing, and the interface remains sharp.

The primary flow has only one non-zero velocity component, which is a function of the radial position *r*. The corresponding governing equation for steady and axisymmetric flow is:

$$\frac{1}{r}\frac{d}{dr}\left[Kr\left|\frac{du}{dr}\right|^{n-1}\frac{du}{dr}\right] = \frac{dp}{dz} \tag{1}$$

The relevant boundary conditions are:
no-slip at the wall:

$$u\big|_{R_2} = 0 \tag{2}$$

velocity continuity at the interface:

$$u\big|_{r\to R_1^-} = u\big|_{r\to R_1^+} \tag{3}$$

continuity of shear stress at the interface:

$$K_1\left(\frac{du}{dr}\right)^{n_1}\Bigg|_{r\to R_1^-} = K_2\left(\frac{du}{dr}\right)^{n_2}\Bigg|_{r\to R_1^+} \tag{4}$$

Integration of equation (1) and the use of the boundary condition in Equation (4) results in:

$$\left|\frac{du}{dr}\right|^{n} = \frac{r}{2K\varepsilon}\frac{dp}{dz} \tag{5}$$

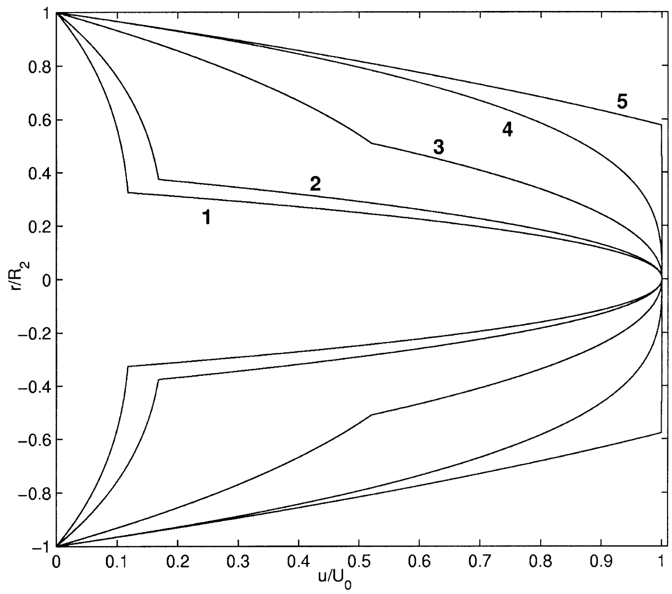

Figure 6. Velocity profiles for two co-flowing, concentric power-law liquids with volume flux $Q_1 = Q_2 = 1.6$ cm^3/s for varying power-law parameters *n* and *K*.

where ε is a sign coefficient, which is 1 or -1, depending upon the sign of *du*/*dr*. Note that the absolute value sign may be dropped because *du*/*dr* is always negative in pipe flow, thus:

$$-\frac{du}{dr}=\left[\frac{r}{2K}\left(-\frac{dp}{dz}\right)\right]^{\frac{1}{n}} \tag{6}$$

A second integration and the use of the boundary conditions in Equations (2 to 4) yields:

$$u_1=\frac{n_1}{n_1+1}\left[\frac{1}{2K_1}\left(-\frac{dp}{dz}\right)\right]^{\frac{1}{n_1}}\left(R_1^{\frac{n_1+1}{n_1}}-r^{\frac{n_1+1}{n_1}}\right)+$$

$$\frac{n_2}{n_2+1}\left[\frac{1}{2K_2}\left(-\frac{dp}{dz}\right)\right]^{\frac{1}{n_2}}\left(R_2^{\frac{n_2+1}{n_2}}-R_1^{\frac{n_2+1}{n_2}}\right) \tag{7}$$

$$u_2=\frac{n_2}{n_2+1}\left[\frac{1}{2K_2}\left(-\frac{dp}{dz}\right)\right]^{\frac{1}{n_2}}\left(R_2^{\frac{n_2+1}{n_2}}-r^{\frac{n_2+1}{n_2}}\right)$$

$$\left(R_1\le r\le R_2\right) \tag{8}$$

Using the following definitions:

$$\frac{R_1}{R_2}=k,\qquad \frac{Q_1}{Q_2}=q \tag{9}$$

where *k* is the radius ratio and *q* is the volume flux ratio, Equation (7) may be rewritten as:

$$u_1=U_0-\frac{n_1}{n_1+1}\left[\frac{1}{2K_1}\left(-\frac{dp}{dz}\right)\right]^{\frac{1}{n_1}}r^{\frac{n_1+1}{n_1}} \tag{10}$$

where U_0 is the centerline velocity given by:

$$U_0=\frac{n_1}{n_1+1}\left[\frac{1}{2K_1}\left(-\frac{dp}{dz}\right)\right]^{\frac{1}{n_1}}R_1^{\frac{n_1+1}{n_1}}+$$

$$\frac{n_2}{n_2+1}\left(1-k^{\frac{n_2+1}{n_2}}\right)\left[\frac{1}{2K_2}\left(-\frac{dp}{dz}\right)\right]^{\frac{1}{n_2}}R_2^{\frac{n_2+1}{n_2}} \tag{11}$$

and the pressure drop is given by:

$$\frac{dp}{dz}=-2K_2\left(\frac{n_2+1}{n_2}\frac{Q_2}{\pi}\right)^{n_2}R_2^{-3n_2-1}\left[1-k^2-\frac{2n_2}{3n_2+1}\left(1-k^{\frac{3n_2+1}{n_2}}\right)\right]^{-n_2} \tag{12}$$

From the above analysis, it is apparent that the system is completely defined by specifying *dp*/*dz*, the flow rates, and the properties of the fluids. In other words, the radius ratio *k* is automatically determined if the other parameters are specified. We define viscosity ratio *m* as $m = \mu_1/\mu_2$, where μ is nominal viscosity at the average strain rate. For our cases, average strain rate is calculated using the following equation:

$$\left(\frac{du}{dr}\right)_{avg}=2\frac{\int_0^{R_1}\frac{du_1}{dr}rdr+\int_{R_1}^{R_2}\frac{du_2}{dr}rdr}{R_2^2} \tag{13}$$

Figure 6 shows the analytically derived velocity profiles for five pairs of power-law liquids (corresponding *K* and *n* are listed in Table 2) with $Q_1 = Q_2 = 1.6$ cm^3/s and $R_2 = 1.27$ cm. From this plot, it is obvious that when the inner fluid is less-viscous than the outer fluid, then the outer, more-viscous liquid is relatively stagnant, whereas the inner, less-viscous liquid moves as a high-speed core. Conversely, when the inner fluid is more-viscous than the outer fluid, the outer less viscous liquid shears easily over the pipe wall, and carries the inner more viscous liquid which behaves essentially as a plug flow. In particular, for identical liquids ($K_1 = K_2$ and $n_1 = n_2$), the profile exhibits a simple power-law behaviour for the entire pipe cross section, as expected (Curve 4).

For the special case when both liquids are Newtonian ($n_1 = n_2 = 1$), Equations (7) and (8) simplify as:

$$u_1=\frac{1}{4\mu_1}\frac{dp}{dz}\left(r^2-R_1^2\right)+\frac{1}{4\mu_2}\frac{dp}{dz}\left(R_1^2-R_2^2\right)\qquad\left(0\le r\le R_1\right) \tag{14}$$

Table 2. Power-law parameters K and n in Figure 6.

Curve 1	$K_1 = 0.04$	$n_1 = 0.9$	$K_2 = 0.75$	$n_2 = 0.5$
Curve 2	$K_1 = 0.05$	$n_1 = 1.0$	$K_2 = 0.5$	$n_2 = 0.5$
Curve 3	$K_1 = 0.05$	$n_1 = 0.9$	$K_2 = 0.1$	$n_2 = 0.75$
Curve 4	$K_1 = 0.75$	$n_1 = 0.5$	$K_2 = 0.75$	$n_2 = 0.5$
Curve 5	$K_1 = 0.5$	$n_1 = 0.5$	$K_2 = 0.05$	$n_2 = 5$

$$u_2 = \frac{1}{4\mu_2}\frac{dp}{dz}\left(r^2 - R_2^2\right) \qquad \left(R_1 \le r \le R_2\right) \tag{15}$$

and the pressure drop is given by:

$$\frac{dp}{dz} = -\frac{8Q_2\mu_2}{\pi R_2^4}\frac{1}{\left(1-k^2\right)^2} \tag{16}$$

It is apparent that the system is completely defined by specifying dp/dz, q, and m. In other words, the radius ratio k is automatically determined if the other parameters are specified. The radius ratio k is given by:

$$k = \left[\frac{(1+q) \pm \sqrt{1+\frac{q}{m}}}{2+q-\frac{1}{m}}\right]^{1/2} \tag{17}$$

Figure 7 shows the analytically derived velocity profiles for two Newtonian liquids such that the volume flow rate ratio q is fixed at 1. The liquids exhibit relative mobilities that are similar to the power-law liquids for various values of m. In particular, for $m = 1$ (identical liquids), the profile reduces to a simple parabola as expected.

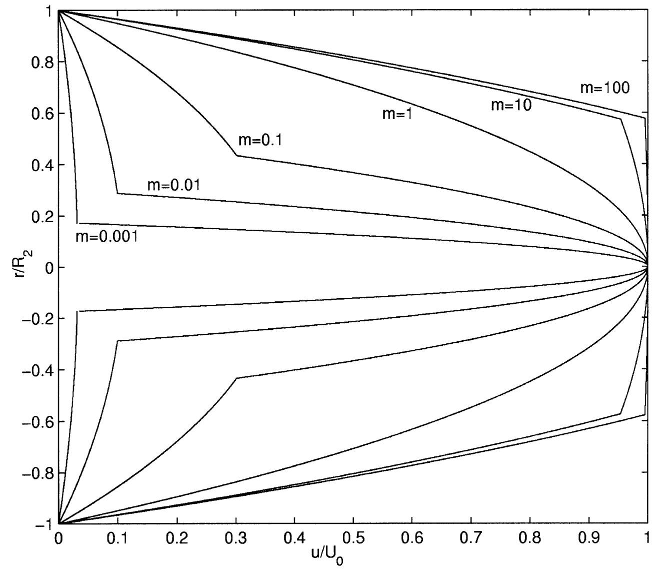

Figure 7. Velocity profiles for two co-flowing, concentric Newtonian liquids with volume flux ratio $q = 1$ for varying viscosity ratios m.

Flow Patterns using LIF

The flow is characterized by the Reynolds number Re, which is based on the mean velocity of the combined core-flow and co-flow $\bar{U}$, the radius of the tube R_2, and the nominal kinematic viscosity of inner fluid ν_1.

$$Re = \frac{2\bar{U}R_2}{\nu_1} \tag{18}$$

The effect of increasing Re is depicted in Figures 8 and 9. Here, the inner and outer liquids are samples 4 and 1 respectively (see Figure 2). For the case of Re = 20, the viscosity at the core region is 8 mPa·s, the viscosity ratio is 1/24, and volume flow rates of the two liquids are $Q_1 = Q_2 = 1.6$ mL/s. Figure 8 shows a stable case for small Reynolds number (Re = 0.2). When Re = 6.7, a way core-flow with fissures was observed (figure 9). Wavy flow with fissures was obtained again at Re = 13, but it was a little more unstable. At Re = 20, a new pattern of wavy core-flow with core break up was observed. The flow became more unstable, with enhanced break up at Re = 27. The amplitude of the instability increased further for Re = 40.

Figures 10 and 11 show the intensity distributions obtained from LIF frames for stable and unstable cases using:

$$\bar{I}(r) = \frac{1}{C}\frac{1}{N}\sum_{i=1}^{N}\sum_{c=1}^{C} I(i,c,r) \tag{19}$$

$$\sigma_I(r) = \sqrt{\frac{1}{C}\frac{1}{N}\sum_{i=1}^{N}\sum_{c=1}^{C}[I(i,c,r) - \bar{I}(r)]^2} \tag{20}$$

where i, c, and r are indices for frame, column, and row, N is the number of frames, C is the number of columns, I is the intensity, $\bar{I}$ is the mean value, and σ_I is the RMS value. For the stable case in Figure 10, the inner and outer liquids are samples 3 and 2 (see Figure 2) respectively, the viscosity at the core region is 27 mPa·s, the viscosity ratio is 1/3, and volume flow rates of the two liquids are 0.02 mL/s. The Reynolds number is 0.07. In Figure 10, $C = 1000$, and $N = 100$. Both curves are normalized by the maximum value of $\bar{I}$. The mean profile indicates a wide plateau towards the middle of the pipe with steeply descending sides. In fact, the plot of $\bar{I}$ approximates a top-hat profile, which would result in the complete absence of diffusion and instability-induced oscillation. The σ_I profile indicates small values throughout, with minor but noticeable peaks at the interface. Apparently, although the flow seems to belong to the stable regime, a small instability is still present in Figure 10. This small instability contributes to the deviation of the $\bar{I}$ profile from a top-hat. Molecular diffusion is very small due to the small residence time involved and does not contribute significantly to the smoothing of the $\bar{I}$ profile at the interface.

In Figure 11 (unstable case), $C = 1000$, and $N = 3$. The fluid properties and flow parameters for the five profiles in Figure 11 are the same as in Figure 9. It is immediately obvious that both $\bar{I}$ and σ_I plots are completely different when a strong instability

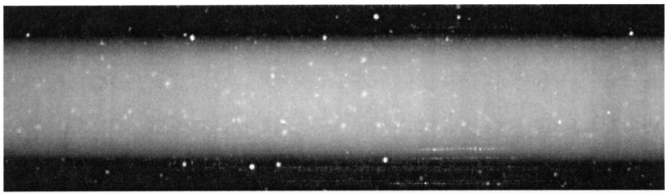

Figure 8. LIF image for viscosity ratio m = 1/24 and volume flow rate ratio q = 1 with vanishing Reynolds number (stable case, Re = 0.2). Note that this image displays the region $r < R_2/2$.

is present. $\overline{I}$ now resembles a Gaussian distribution rather than a top-hat, and the σ_I values are very large. Due to the small residue time involved, molecular diffusion cannot account for the reduced radial intensity gradient at the interface; in fact, it is solely attributable to the strong instability. The waving of the core-flow helps to distribute the dye in the radial direction, lowering the intensity for $r/R_2 < k$ and increasing it for $r/R_2 > k$. Furthermore, the waving of the core-flow causes an axial variation in intensity which is also reflected in the strongly elevated σ_I values at the interface. The strength of the instability is clearly seen to increase with Re, as evidenced by the increase in RMS values. The normalized peak value of σ_I at Re = 6.7 is about 0.35, whereas it increases monotonically to about 0.45 for Re = 40. Similarly, the centerline value of σ_I increases from 0.15 to 0.3 as the Re increases from 6.7 to 40.

PIV Results of Velocity Profile

PIV was first applied to a stable baseline flow to verify the measured profile against the analytical result. The chosen flow is the same as in Figure 10. The flow rates of the two liquids were adjusted to the desired value and several minutes were permitted for steady conditions to be established. Images were recorded subsequently. Figure 12 is the PIV result for the stable case and is the average of 20 frames. This figure compares the experimental velocity profile with the exact solution given by Equations (8) and (9). We focused our attention on a 19-mm (75% of pipe diameter) square area centered along the pipe axis during experimental measurements. The exact solution was obtained for all diameter values. In the core region, we can see that the experimental and the exact solution match well. However, at the liquid interface, the exact solution shows a sharp change of gradient, while the experimental results indicate a smoother transition. This may be due to two reasons: (1) the PIV technique contributes to smoothing due to the inherent spatial averaging during the process of computing correlating functions to determine velocity, and (2) a very small instability might be present despite visual evidence to the contrary. As stated earlier, molecular diffusion across the interface is much too small to contribute to the smoothing of velocity profile. We estimate (1) to be the dominant cause for the smoothing at the interface.

An instantaneous PIV vector map for the unstable case is shown in Figure 13. The core viscosity is 8 mPa·s, the viscosity ratio is 1/24, and volume flow rates are $Q_1 = Q_2$ = 1.0 mL/s. The Reynolds number is 13. The flow is from left to right. The wavy shape of the flow and strong instability are clearly evident. Figure 14 shows the averaged PIV results for three unstable cases. Each of the three profiles is an average of 30 PIV frames.

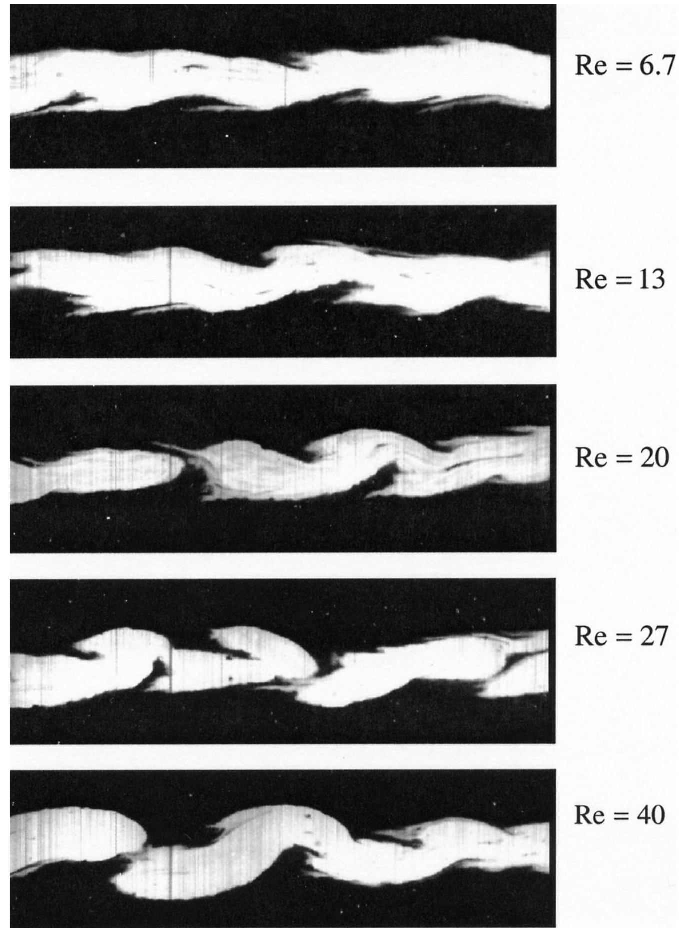

Figure 9. LIF images for viscosity ratio m = 1/24 and volume flow rate ratio q = 1 (unstable cases).

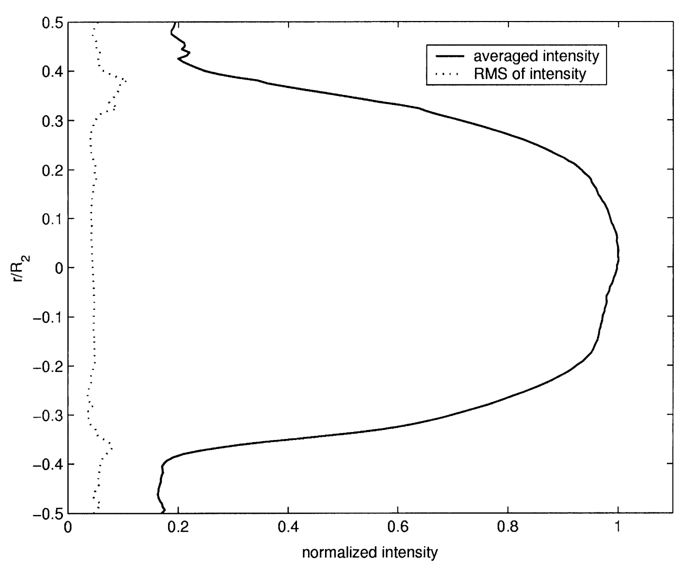

Figure 10. Mean and RMS values of intensity of LIF frames for stable case (Re = 0.07).

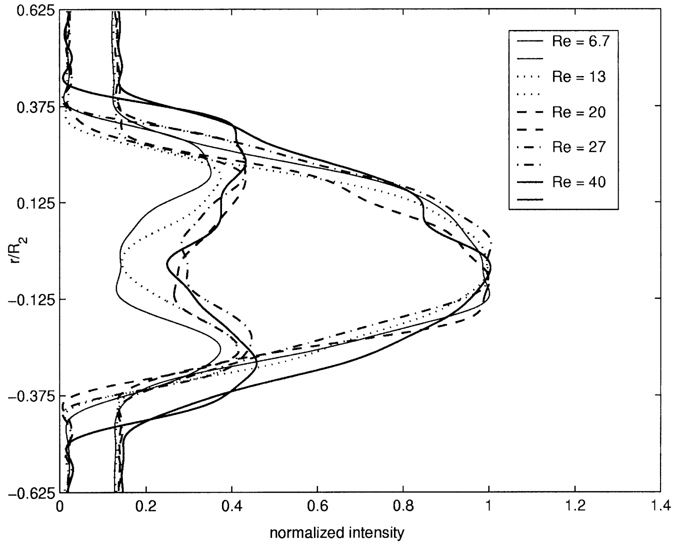

Figure 11. Mean and RMS values of intensity of LIF frames for unstable cases.

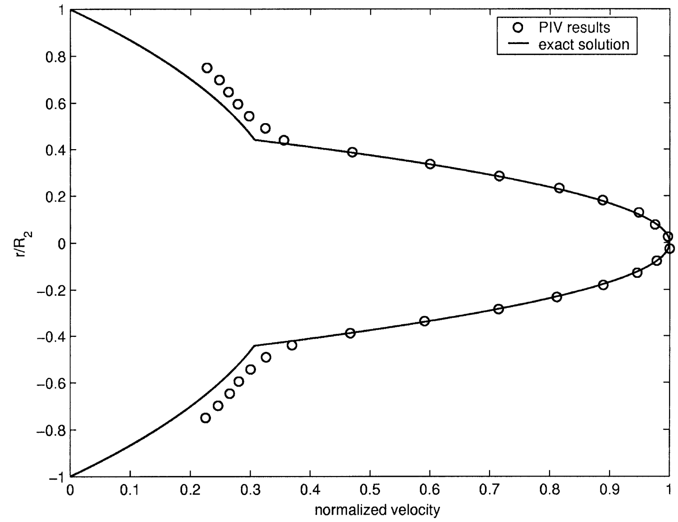

Figure 12. Comparison of PIV stable results with exact stable solution (Re = 0.07).

Furthermore, the data were averaged along rows to produce the ensemble-averaged radial velocity profile. The viscosity at the core region is 8 mPa·s, the viscosity ratio is 1/24, and volume flow rates of the two liquids are identical. The Reynolds numbers were 13, 20, and 27 respectively. For all the four profiles, the nominal radius ratios were the same. Unlike the PIV results for the stable case (Figure 12), the unstable results in the core region were clearly different from the stable solution. Due to the waviness of central high-speed jet, the time-averaged centerline velocity is smaller than the corresponding stable centerline velocity. Because the area under the curve is the same for all the cases (since q is the same) the outer flow speeds up slightly to compensate for the slower flow at the centerline. This plot clearly shows the time-averaged effect of the strong instability.

Figure 15 shows the mean and RMS of axial velocity ($\bar{U}$ and σ_U) for the stable case (same parameters as in Figure 12). Figure 16 presents $\bar{U}$ and σ_U for the unstable case corresponding to Re = 13 in Figure 14. Equations (19) and (20) are used to calculate the mean and RMS respectively (with I replaced by U). In Figure 15, C = 30, and N = 20. Both curves are normalized

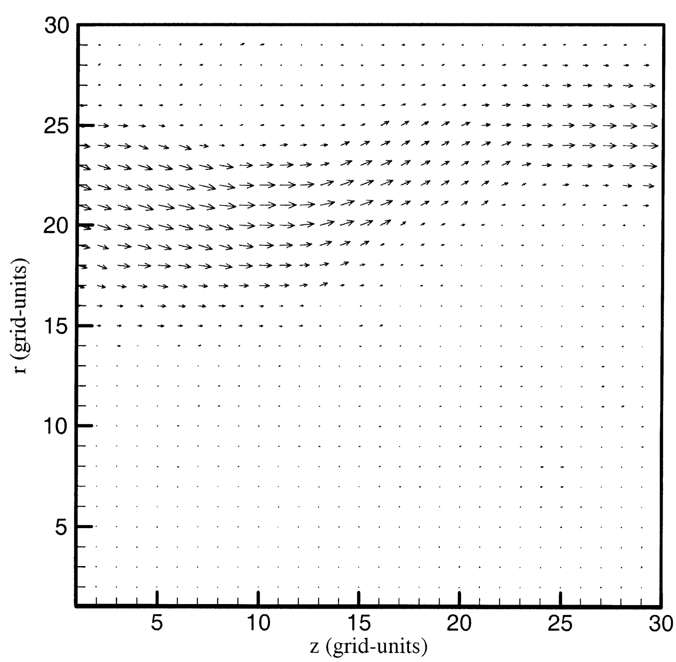

Figure 13. Instantaneous PIV picture for m = 1/24, q = 1, and Re = 13 (1 grid-unit = 0.63 mm).

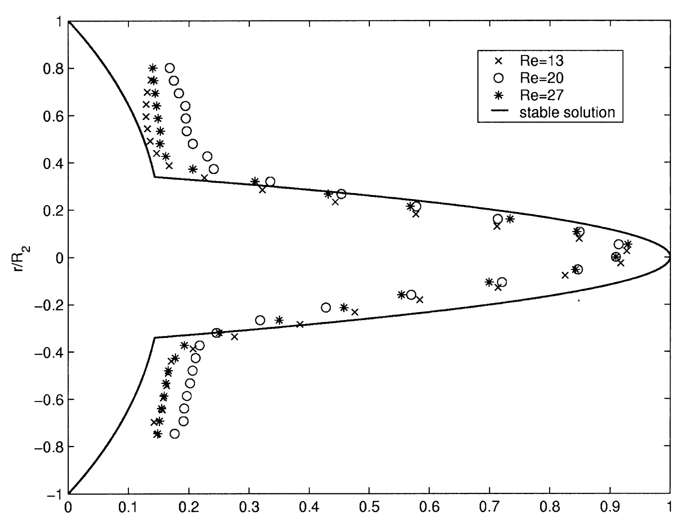

Figure 14. Comparison of PIV unstable results with exact stable solution.

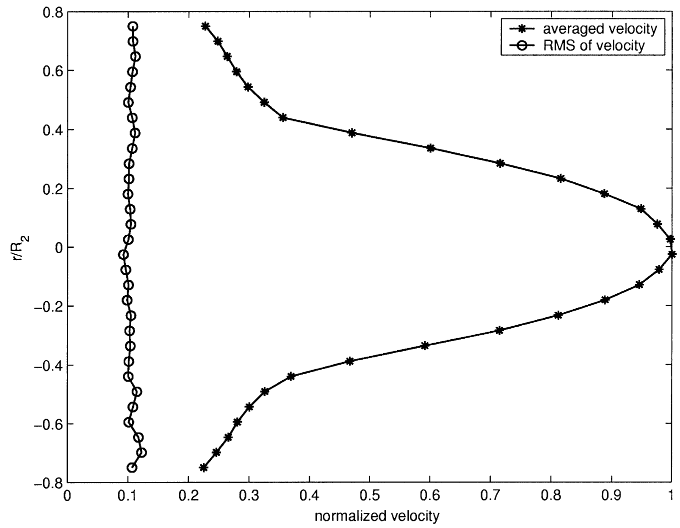

Figure 15. Mean and RMS values of axial velocity for a stable case (Re = 0.07).

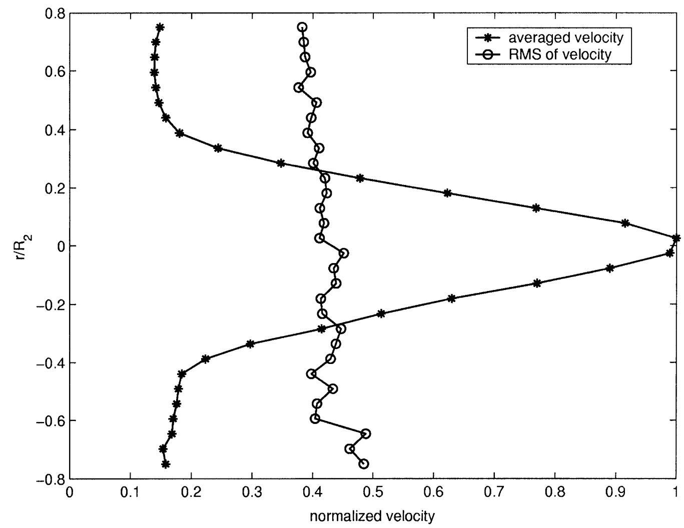

Figure 16. Mean and RMS values of axial velocity for anunstable cases (Re = 13).

by the maximum value of $\bar{U}$. The RMS profile indicates small values of about 0.1, implying that a small instability may still be present in Figure 13, although flow visualization indicates that the flow is apparently stable. Note that the RMS error inherent to the PIV measurement is only about 2 to 4% of the centerline velocity, therefore a measured RMS of 10% is indicative of a small unsteadiness even in the stable flow.

In Figure 16, C = 30, and N = 30. Unlike the stable case, the normalized RMS values are quite large (about 0.4). The sharp increase in σ_U is consistent with the instantaneous PIV realization in Figure 11 and the LIF image in Figure 9. The waviness of the high-speed core causes large temporal fluctuations in the U velocity at any given radial location, leading to large values of σ_U.

Figures 17 and 18 present the mean and RMS for the radial velocity ($\bar{V}$ and σ_v) for the stable and unstable cases corresponding to Figures 15 and 16 respectively. As expected, $\bar{V}$ is very small for both stable and unstable cases (about 1% of the maximum $\bar{U}$ velocity). Such small values indicate that the time-averaged flow is horizontal as expected, and provides a useful check on the PIV technique. On the other hand, σ_v experiences a sharp rise when the instability is operating ($\sigma_v/\bar{U}_{max} \approx 0.17$ for the unstable case compared to about 0.06 for the stable case). The increase in σ_v is again attributed to the waviness of the core-flow.

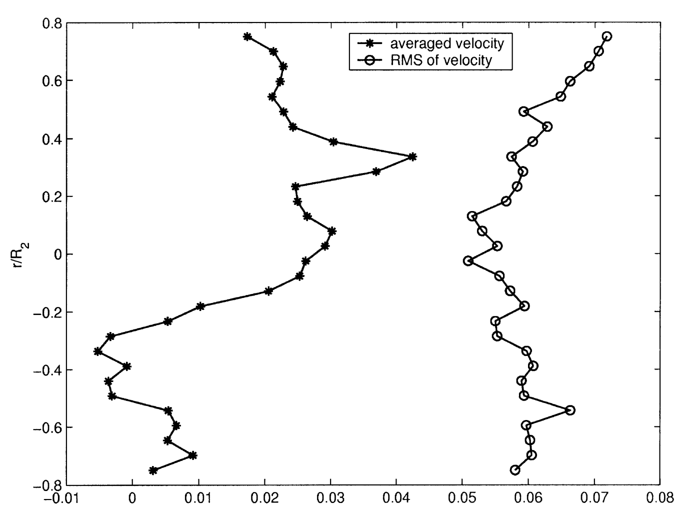

Figure 17. Mean and RMS values of radial velocity for a stable case (Re = 0.07).

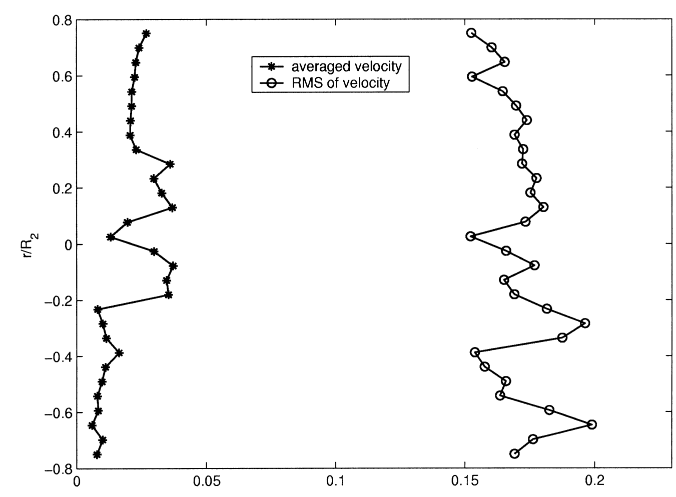

Figure 18. Mean and RMS values of radial velocity for an unstable cases (Re = 13).

Conclusions

Experiments were conducted to investigate instabilities during centerline injection of a lower-viscosity liquid into a higher-viscosity miscible co-flow in a pipe. LIF and PIV were used to visualize and quantify the flow field. An analytical study of axisymmetric immiscible power-law co-flow is also presented. A comparison of experimental stable cases and exact solutions revealed that there might exist an interfacial layer, which smoothes out the discontinuity of the velocity gradient at the interface. The unstable region exhibits different modes depending on the viscosity ratio, volume flux ratio, and Reynolds number. Two kinds of modes were observed: (1) wavy core-flow with fissures, and (2) wavy core-flow with core break-up. The time-averaged experimental velocity profiles for the unstable core indicate a broadening of the jet at the centerline which is consistent with the LIF visualization. The measured values of and indicate the strength σ_u of σ_v the instability.

Acknowledgements

This work was partially supported by a Dupont Educational Aid Grant, and a Dupont/Delaware Research Partnership Grant. The support of Drs. D. Massouda and E. Guertin (Dupont) is gratefully acknowledged.

Nomenclature

c	index for column
C	number of columns
D	tube diameter, (m)
De	Deborah number (= τ/t_f)
i	index for frame
I	intensity
$\bar{I}$	mean value of intensity
k	radius ratio, (mPa·s^m)
K	power-law parameter
m	viscosity ratio
n	power-law parameter
p	static pressure, (Pa)
q	volume flux ratio
Q	volume flux, (m^3/s)
r	radial coordinate, (m)
r	index for row
R	radius, (m)
Re	Reynolds number defined by equation (13)
t_f	flow time constant, (s)
u	axial velocity, (m/s)
U	average axial velocity, (m/s)
U_0	centerline velocity, (m/s)
$\bar{U}$	mean value of axial velocity of combined core-flow and co-flow, (m/s)
$\bar{U}_{max}$	maximum value of $\bar{U}$, (m/s)
V	averaged radial velocity, (m/s)
$\bar{V}$	mean value of radial velocity of combined core-flow and co-flow, (m/s)
z	axial coordinate, (m)

Greek Symbols

γ_ι	interfacial tension, (N/m)
μ	nominal viscosity, (Pa·s)
ν	nominal kinematic viscosity, (m^2/s)
ρ	density, (kg/m^3)
σ_I	RMS value of intensity
σ_U	RMS value of axial velocity, (m/s)
σ_V	RMS value of radial velocity, (m/s)
τ	relaxation time of fluid, (s)

Subscripts

1	inner fluid (core-flow)
2	outer fluid (co-flow)

References

Bai, R., K. Chen and D.D. Joseph, "Lubricated Pipelining: Stability of Core-annular Flow. Part V: Experiments and Comparison with Theory", J. Fluid Mech. **240**, 97–132 (1992).

Charles, M.E., G.W. Govier and G.W. Hodgson, "The Horizontal Pipeline Flow of Equal Density Oil-water Mixtures", Can. J. Chem. Eng. **39**, 27–36 (1961).

Charru, F. and J. Fabre, "Long Waves at the Interface Between two Viscous Fluids", Phys. Fluids **63**, 1223–1235 (1994).

Guertin, E.W., Private communication (1997).

Hickox, C.E., "Instability Due to Viscosity and Density Stratification in Axisymmetric Pipe Flow", Phys. Fluids **14**, 251–262 (1971).

Joseph, D.D., M. Renardy and Y. Renardy, "Instability of the Flow of Immiscible Liquids with Different Viscosities in a Pipe", J. Fluid Mech. **141**, 309–317 (1984).

Kao, T.W. and C. Park, "Experimental Investigations of the Stability of Channel Flows. Part 2. Two-layered Co-current Flow in a Rectangular Channel", J. Fluid Mech. **52**, 401–423 (1972).

Li, C. –H., "Instability of Three-layer Viscous Stratified Flow", Phys. Fluids **12**, 2473–2481 (1969).

Prasad, A.K., "Particle Image Velocimetry", Current Science **79**, 51-60 (2000).

Ranganathan, B.T. and R. Govindarajan, "Stabilization and Destabilization of Channel Flow by Location of Viscosity-stratified Fluid Layer", Phys. Fluids **131**, 1–3 (2001).

Renardy, Y. and D.D. Joseph, "Couette-Flow of 2 Fluids Between Concentric Cylinders", J. Fluid Mech. **150**, 381–394 (1985).

Streiff, F.A. and J.A. Rogers, "Don't Overlook Static-mixer Reactors", Chem. Eng.s **101,** 76–82 (1994).

Ventresca, A., Q. Cao and A.K. Prasad, "The Influence of Viscosity Ratio on Mixing Effectiveness in a Two-fluid Laminar Motionless Mixer", Can. J. Chem. Eng. **80**, 614–621 (2002).

Yih, C.-S., "Instability Due to Viscosity Stratification", J. Fluid Mech. **26**, 337–352 (1967).

Manuscript received November 15, 2001; revised manuscript received January 16, 2003; accepted for publication April 10, 2003.